Available online at www.sciencedirect.com
ScienceDirect
Journal of Sound and Vibration 324 (2009) 666–689
JOURNAL OF SOUND AND VIBRATION
www.elsevier.com/locate/jsvi

Effects of train impacts on urban turnouts: Modelling and validation through measurements

S. Bruni[a], I. Anastasopoulos[b], S. Alfi[a,*], A. Van Leuven[c], G. Gazetas[b]

[a]*Department of Mechanical Engineering, Politecnico di Milano, Milan, Italy*
[b]*School of Civil Engineering, National Technical University of Athens, Athens, Greece*
[c]*D2S International, Brussels, Belgium*

Received 21 July 2008; received in revised form 5 December 2008; accepted 16 February 2009
Handling Editor: C.L. Morfey
Available online 3 April 2009

Abstract

Train–track interaction at turnouts is a main issue in the design and maintenance of railway systems. Due to the particular geometry of wheel–rail contact and to the sudden variation of track flexibility, severe impact loads may occur during train passage over the turnout. In this paper, two different modelling approaches to reproduce train–turnout interaction are proposed and compared. A first technique, developed by Politecnico di Milano, is based on a detailed multi-body model of the trainset and of wheel–rail contact, whereas for the turnout structure a simplified finite element model is used. The second modelling technique, developed by the National Technical University of Athens, relies on a detailed finite element model of the turnout, while a simplified model is used to compute impact loading due to wheel passage. In this paper the two methods are validated trough comparison with line measurements performed on turnout systems from three different urban railway networks.

1. Introduction

Train–track interaction at turnouts is a main issue in the design and maintenance of railway systems. Due to the particular geometry of wheel–rail contact and to the sudden variation of track flexibility, severe impact loads may occur when wheels pass over the switch toe and across the gap in the crossing nose. Dynamic loading is the cause of short turnout service life, increase of maintenance costs and severe noise and vibration disturbance. The latter is of particular importance for urban railway lines developing in densely populated environments.

In order to reduce dynamic loading, appropriate design of the turnout and of its foundation is required, involving several issues such as the geometry of the rail profiles, flexibility and dynamic impedances of its components, resilience and damping of the foundation system (either on ballast, or of special anti-vibration design to minimise the transmission of ground borne vibrations). Furthermore, the change of wheel and rail

*Corresponding author.
E-mail addresses: stefano.bruni@polimi.it (S. Bruni), ianast@civil.ntua.gr (I. Anastasopoulos), stefano.alfi@polimi.it (S. Alfi), andre.vanleuven@d2sint.com (A. Van Leuven), gazetas@ath.forthnet.gr (G. Gazetas).

0022-460X/$ - see front matter © 2009 Elsevier Ltd. All rights reserved.
doi:10.1016/j.jsv.2009.02.016

original geometry produced by wear and plastic deformation strongly affects wheel–rail interaction and the severity of impacts, so that turnout performance may deteriorate substantially with the increase of wear: this is another point that has to be carefully considered in the study of train–turnout interaction and in the design of turnout systems.

Despite of the aforementioned geometrical complexities of turnouts compared to standard tracks, mathematical models of train–track interaction can be employed to simulate impact and vibration effects on turnouts, allowing for performance optimisation and development of innovative concepts to reduce life cycle costs and vibration-induced nuisance of people living in the proximity of urban railway lines.

Until today, a rather large number of studies have appeared in the scientific literature considering the situation of a train running on a turnout, but mainly from the point of view of low frequency train–turnout interaction (limited to 20–30 Hz, in this context): i.e., the effect of local turnout geometry on vehicle dynamics [e.g., 1,2,3]. However, to the best of our knowledge, the dynamic flexibility of the turnout is either neglected or represented by simplified models, and the analysis focuses on vehicle motion and ride safety problems.

Andersson and Dahlberg [4,5] pioneered in studying train–turnout interaction in a wider frequency range (up to some hundreds Hz), addressing impact effects on the crossing by introducing a finite element schematisation for the turnout which makes use of beam elements to represent rails and sleepers, and of lumped parameter elements to represent railpads and ballast. In their study, which is confined to vertical dynamics, modal condensation is used to limit the degrees of freedom of the turnout; vehicle dynamics are represented through a simplified half-bogie model, in which the wheelset and the half bogie are considered as rigid bodies, therefore neglecting the high frequency component associated with the flexibility of the wheelset. More recently, Kassa et al. [6–8] expanded this approach to consider vertical and lateral vibration of the train–turnout system: the track model is approximately the same as in Ref. [4,5] whereas the vehicle model consists of a rigid bogie frame and two rigid wheelsets, connected through linear springs and dampers representing the primary suspensions, but neglecting the effect of wheelset flexibility.

This paper develops and compares two alternative approaches for numerical simulation of train–turnout interaction in a frequency range up to 500 Hz. The first approach, developed by Politecnico di Milano, is based on a multi-body model of the vehicle, a detailed model of wheel–rail contact, and a finite element model for the turnout where use is made of beam-type finite elements. The second approach, developed by the National Technical University of Athens, is based on a detailed 3-D finite element model of the turnout and taking account of soil–foundation interaction, whereas a simplified model is used to represent impact loading produced by wheel passage. The two modelling techniques can be considered as complementary, since the first focuses on the local wheel–rail interface, whereas the second provides a more detailed description of the propagation of ground borne vibration within the body of the turnout and through the surrounding soil. The two approaches were developed in the course of the FP6 funded research project "*TURNOUTS*", aiming at the improvement of existing urban rail turnouts through the development of new concepts. One of the main goals of the project was the reduction of noise and vibration, and of the associated maintenance costs.

In the same project, line measurements were performed on different types of urban turnouts, to allow for validation of the developed numerical simulation methods and of new turnout concepts. This paper utilises those measurements as a yardstick to assess the accuracy of the two modelling approaches. In order to cover a wide range of typical loading conditions of urban lines, three validation cases are considered: one from a metro line, and two from tramway lines. The three validation cases are characterized by different service conditions, regarding the type of rolling stock into service, vehicle axle loads, maximum negotiation speed, and the degree of wear. The comparisons reported herein (see Section 4) demonstrate the effectiveness and robustness of the two modelling approaches: both methods yield comparable results in terms of turnout vertical acceleration at the crossing nose, in very good agreement with the corresponding line measurements.

The final part of the paper (Section 5), summarizes the main findings of a parametric sensitivity study, dealing with the effect of the main geometrical and structural turnout parameters on turnout performance (i.e., the impact effects occurring at the crossing). The results from this analysis were used within the *TURNOUTS* project to design and fine-tune new turnout concepts that minimise impact effects and vibration and noise transmission in urban turnout systems [9].

2. Numerical models of train–turnout interaction

Two alternative approaches were developed for modelling impact and vibration effects produced by train passage over a turnout system. The first one, referred to as "Method A", is based on a detailed multi-body model of the trainset and of wheel–rail contact in presence of spatially varying rail profiles, while a simplified beam-type finite element model is used for the turnout structure. The second alternative approach ("Method B") focuses on a detailed finite element model of the turnout, whereas the passing train and the mechanism of train–turnout interaction are represented in a simplified way.

2.1. Multi-body model of train turnout interaction (Method A)

The first modelling approach is based on the coupling of a multi-body model of the entire trainset with a finite element model of the track, as summarised in this section; full details on the equations of the model are provided in Ref. [10]. The trainset is decomposed into several modules, representing the car bodies and bogies (each bogie being composed by three bodies, the bogie frame and two wheelsets). For each module, the equations of motion are written with respect to a local moving frame travelling along the ideal path of the module, defined by the geometry of the line. The trainset equations are linearised with respect to kinematic nonlinear effects, assuming the motion to be a small perturbation around the large motion of the moving reference. For car bodies and bogie frames, a rigid body motion with constant forward speed is assumed, and hence five degrees of freedom per body are introduced. For the wheelsets, a flexible body description based on modal superposition, as described in Ref. [11] is introduced. The overall number of degrees of freedom for the whole trainset typically ranges from few hundreds to some thousands, depending on the number of vehicles in the trainset and on the number of coordinates used for the wheelsets.

The finite element model of the turnout includes the switch panel, closure panel and crossing panel, and additionally two sections of standard track before and after the turnout. The latter have a length of 10–20 sleeper spans each, to establish proper boundary conditions for the turnout model. The complete finite element model of the turnout typically includes 600–1000 nodes, 800–1500 finite elements, and 3000–5000 degrees of freedom. To reduce the complexity of the model, different finite element schemes are used to study the two cases of the train negotiating the main line or the branch line. As an example, Fig. 1a shows the main line model of a standard turnout on ballast with monoblock crossing.

Euler–Bernoulli beam elements are used to model the different rails: switch rail, stock rail, point and wing rails, and check rails. For the switch toe, a sequence of beam elements having different sectional properties is used to account for the variability of the rail section. The crossing nose is represented in a simplified way by beam elements connected by multi-directional springs accounting for the point and splice rails merging into

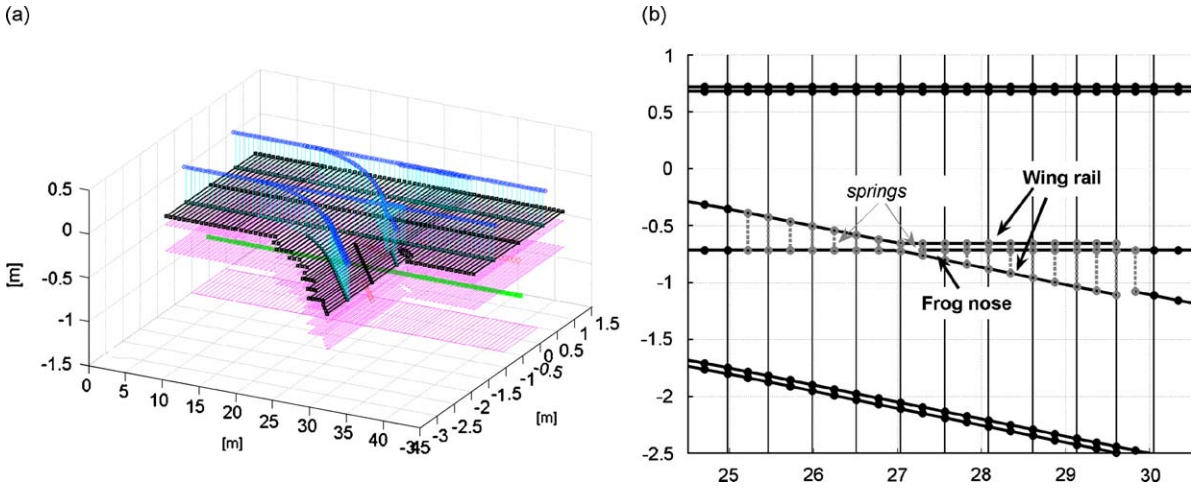

Fig. 1. Method A: global view of the turnout finite element model (a) and detail of the crossing nose model (b).

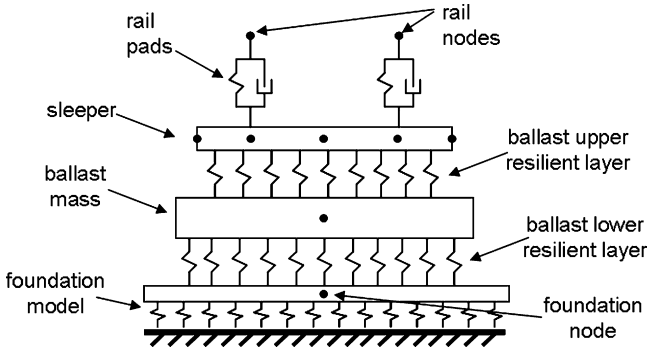

Fig. 2. Method A: track layers modelling in the turnout finite element model.

the nose, see Fig. 1b. When possible, the stiffness parameters for the spring elements are identified based on the comparison of the measured and computed direct inertance of the track at the crossing nose. It shall be pointed out that the use of rigid links instead of springs proved to be inadequate to reproduce the measured track inertance in the frequency range up to 500 Hz.

When modelling a conventional turnout (sleepers on ballast), sleepers are modelled through 4–8 beam elements, rail fasteners through spring-damper elements, and ballast is represented by discrete lumped masses (one below each sleeper) connected to the sleepers and to the foundation of the track by distributed viscoelastic layers. A simplified representation of track foundation flexibility is included in the model, by means of an equivalent beam resting on a viscoelastic layer; parameters for the foundation model were identified based on track inertance measurements performed in the underground railway network of Milano, which were made available from a previous research project. The position of nodes in a typical section of the turnout model is illustrated in Fig. 2.

2.1.1. *Equations of motion*

The equations of motion for the turnout and for the train are written separately. The set of equations governing turnout motion takes the matrix form:

$$\mathbf{M}_T\ddot{\mathbf{X}}_T + \mathbf{C}_T\dot{\mathbf{X}}_T + \mathbf{K}_T\mathbf{X}_T = \mathbf{F}_{TC}(\mathbf{X}_T, \dot{\mathbf{X}}_T, \mathbf{X}_V, \dot{\mathbf{X}}_V) \tag{1}$$

where $\mathbf{X}_T$ and $\mathbf{X}_V$ are, respectively, the vectors of turnout nodal coordinates and of trainset coordinates, $\mathbf{M}_T$, $\mathbf{C}_T$ and $\mathbf{K}_T$ are the mass, damping and stiffness matrices of the turnout finite element model and $\mathbf{F}_{TC}$ is the vector of generalised nodal forces on the turnout corresponding to wheel–rail contact forces.

The equation representing the motion of the trainset passing over the turnout takes the form:

$$\mathbf{M}_V\ddot{\mathbf{X}}_V + \mathbf{C}_V\dot{\mathbf{X}}_V + \mathbf{K}_V\mathbf{X}_V = \mathbf{F}_{IN}(\mathbf{X}_V, \dot{\mathbf{X}}_V) + \mathbf{F}_{INT}(\mathbf{X}_V, \dot{\mathbf{X}}_V) + \mathbf{F}_{VC}(\mathbf{X}_V, \dot{\mathbf{X}}_V, \mathbf{X}_T, \dot{\mathbf{X}}_T) \tag{2}$$

being $\mathbf{M}_V$, $\mathbf{C}_V$ and $\mathbf{K}_V$ the mass, damping and stiffness matrices of the trainset, $\mathbf{F}_{IN}$ the vector of inertial forces caused by the non-inertial motion of the local moving frames taken as reference for the trainset modules, $\mathbf{F}_{INT}$ the vector of internal forces representing the effect of the differential motion of the two local frames associated to modules connected by a suspension element and nonlinear internal forces (e.g., bumpstops), and finally $\mathbf{F}_{VC}$ the vector of generalised forces produced on the trainset by wheel–rail contact forces.

The presence in Eqs. (1) and (2) of nonlinear effects associated with wheel–rail contact and with nonlinear elements in vehicle suspension requires the problem to be solved in the time domain. Furthermore, terms $\mathbf{F}_{TC}$ and $\mathbf{F}_{VC}$, representing in Eqs. (1) and (2) the effect of wheel rail contact forces, are a function of both turnout motion $\mathbf{X}_T, \dot{\mathbf{X}}_T$ and vehicle motion $\mathbf{X}_V, \dot{\mathbf{X}}_V$, and hence introduce a coupling term between the two sets of equations, that need to be solved simultaneously: this is done using the Newmark's implicit scheme modified according to Ref. [12] to introduce in the time step an iterative correction. The computation time required to simulate on a modern PC-type CPU unit train passage over the entire turnout (duration of the run 5–10 s depending on the speed of the train) is in the range of 1–2 h.

2.1.2. Model of wheel–rail contact forces

Wheel–rail contact forces are defined using a multi-Hertzian approach [13], where the formation of multiple contacts between each wheel and the different rails in the turnout may be reproduced. This is a situation which is commonly encountered during turnout negotiation, when the contact with the wheel is transferred from the stock rail to the switch rail, and then from the closure rail to the crossing nose.

The general procedure used to compute contact forces is based on the so-called "tabulated approach": to speed-up simulation time, a geometric analysis of wheel–rail contact along the turnout is performed prior to simulation, defining for different positions of the wheels respective to the track the number and location of "potential" wheel–rail contact points; the geometric parameters of wheel–rail contact for each potential contact point are stored in a contact table (see Refs. [15,16] for details).

During the numerical simulation process, the contact parameters are recovered by table lookup, and for every potential contact point the normal contact force is evaluated by the use of the Hertzian formulae (zero force meaning that the considered contact point is not active). For every active contact point, creep forces are computed based on the values of the normal force and of longitudinal and transverse creepages, using the formulae by Shen et al. [14]. Finally, the different contact force components are projected along a common local track reference and summed over the different contacts active for the same wheel. These values are then transformed into vectors $\mathbf{F}_{TC}$ and $\mathbf{F}_{VC}$ using the principle of virtual work, and considering the kinematic relationship established between rail displacements and the turnout nodal coordinates, and between wheel displacement and trainset coordinates. The detailed description of the general procedure for calculation of wheel–rail contact forces is reported in Ref. [16].

With respect to the above described general procedure, modifications are introduced to account for the specific situation of train–turnout interaction:

(i) Due to the spatial variation of rail profiles along the turnout, the number of potential contacts and the value of wheel–rail contact parameters are changing not only with the lateral wheel–rail displacement, but also with the longitudinal position of the wheel along the track. This requires to define a multidimensional contact table, where contact parameters are filed as function of the longitudinal wheelset position and of the lateral wheelset shift. In the approach described here, the effect of wheel yaw is not accounted for, to avoid excessive complexity in the construction and interpolation of the contact table: this simplifying assumption is not expected to affect significantly the accuracy of the results, except the case when the train is travelling along the branching line of a short radius turnout, a situation which would perhaps justify the on-line calculation of contact parameters;

(ii) On account of the peculiar 3-D geometry of the crossing nose, vertical wheel movement is produced by the sudden change of the wheel–rail contact from the stock rail to the frog nose. This effect is treated by introducing a generalised description of the contact plane direction, where the "classical" contact angle parameter is replaced by a two-component rotation vector, allowing to describe the general inclination of the plane tangent to wheel–rail contact;

(iii) On the switch blade and on the frog nose the passing wheels are suddenly transferred from one rail to another, having different flexibility in vertical and lateral direction, producing important effects of dynamic excitation that have to be accounted properly. Therefore, in the numerical procedure used to compute wheel–rail contact forces, different potential contacts occurring on the same wheel are associated with different beam elements, allowing then to represent the situation of a single wheel contacting more then one rails, having different inertial and flexibility properties.

Full details about the implementation of the wheel–rail contact model for the specific purpose of modelling train–turnout interaction are provided in Ref. [16].

2.2. FEM modelling of train–turnout interaction (Method B)

The second modelling approach focuses on a detailed three-dimensional finite element model of the whole turnout, whereas the passing train and the mechanism of train–turnout interaction are considered using a simplified approach. The 3-D finite element models incorporate the whole turnout, comprising sleepers, rails,

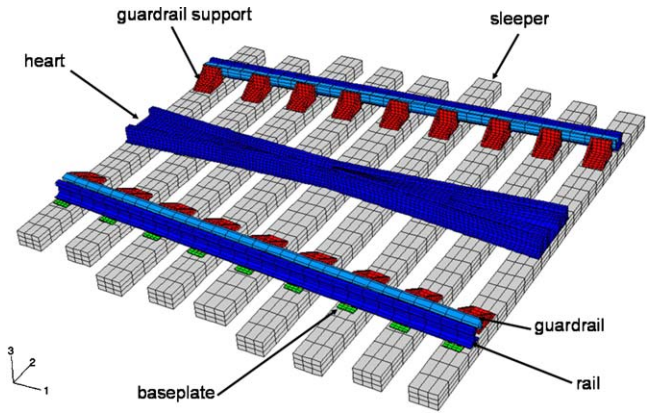

Fig. 3. Method B: the 3-D finite element model for the RATP turnout.

guardrails, crossing nose, railpads, baseplates, and guardrail support plates. The analyses were conducted utilising the finite element code *ABAQUS*. All components were modelled through 3-D hexahedral brick-type elements. The three-dimensional finite element model of the Metro turnout of RATP (used as a reference turnout) is presented in Fig. 3.

While the central sleepers are modelled in 3-D, to incorporate the effect of neighbouring sleepers, as well as of the longitudinal continuation of rails and guardrails, a composite boundary is introduced to the model. It comprises beam elements to model both the neighbouring sleepers and the rail continuation. This way, the central 3-D model is neither assumed fixed at its boundaries, nor taken as free. Waves propagating longitudinally through rails and guardrails are allowed to realistically radiate outside the 3-D model, not affecting its performance. If the boundary was either assumed fixed or free, then such longitudinal waves would be forced to reflect at the boundaries, being trapped inside the model—a rather un-realistic condition. The same holds for vertically propagating waves. In this case, the ballast is providing the means for radiation.

The ballast is modelled through springs and dashpots in all directions (X, Y, and Z). The springs represent the compliance of the ballast, while the dashpots capture radiation damping through the ballast and the supporting soil. If the ballast was placed on top of a rock-type material then radiation damping would be minimal. On the other hand, if the ballast is placed on top of a deformable (resilient) soil layer, the effect of radiation damping can be quite significant.

A simplified analytical model is developed to estimate the dynamic loading onto the turnout. As depicted in Fig. 4, if the geometry of both the turnout's running surfaces as well as of the wheels of the vehicles was perfect, wheel passage over the turnout should almost be of a smooth transition (Fig. 4a). However, assuming that the wheels are worn, and therefore their geometry is not ideal, wheel passage over the turnout will be dominated by impacts and "jumps" of the wheels while passing over the crossing nose (heart) of the turnout, instead of a smooth transition (Fig. 4b).

Such an assumption can be considered to be more realistic, compared to the ideal case of a perfect conical shape of the wheels. The perfect shape assumption may be realistic for the case of new vehicles or for wheels that have recently been rehabilitated. Even in this case, however, the turnout surface cannot always be perfect. Again, such a case will exist only when the turnout is new or after it has been refurbished. So, the assumption of a perfect contact will be valid for comparatively short time periods, during which both the turnout and the wheels are new, in the general sense. Furthermore, since several (different) trains pass over a turnout it is almost impossible that all of them will be equipped with perfect wheels. Therefore, the intersection of the time periods during which the turnout surfaces are perfect with time periods that the passing wheels are also perfect, yields comparatively short time periods for which both conditions are met. The exact extent of the wear w of the wheels and that of the turnout can only probabilistically be estimated. In this paper, we assume that a substantial degree of wear exists.

To compute the impact velocity of the wheel as well as the impact point, an analytical procedure based on a simplified lumped-mass model has been developed. The simplified model takes into account the primary suspension characteristics, the wheel mass, the total weight and the running velocity of the vehicle, and the

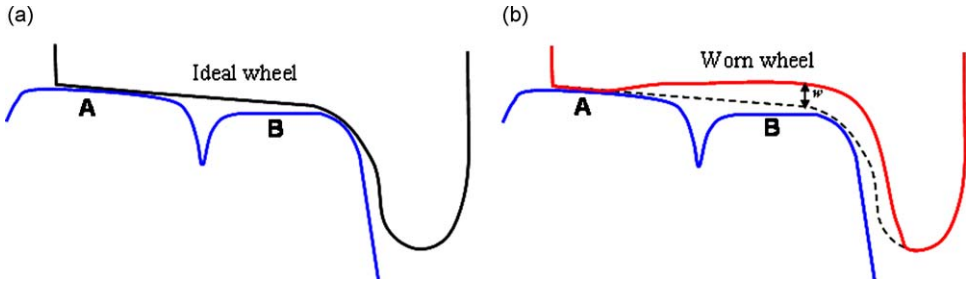

Fig. 4. Wheel passing over the crossing nose of the turnout: (a) new wheel—ideal case, (b) worn wheel—realistic case.

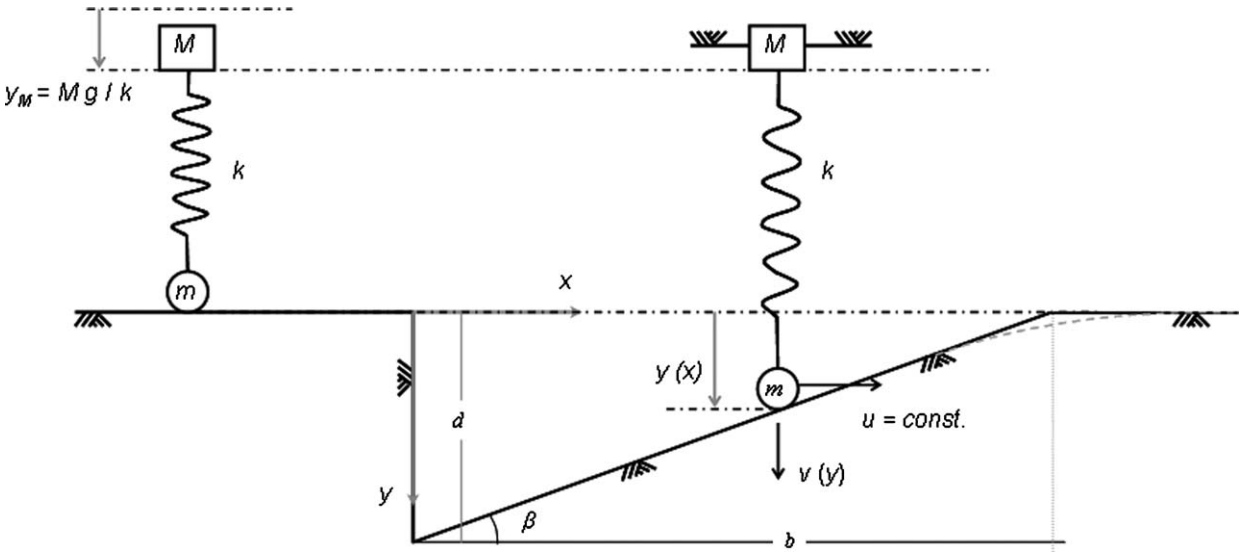

Fig. 5. Method B: simplified modelling of the wheelset impact to the rail.

degree of wear of the wheels of the vehicle and of the running surfaces of the turnout. As illustrated in Fig. 5, the model simulates the "fall" of the wheel (which is due to the inherent imperfections) onto the flange-way gap. When the train passes over the crossing nose of the turnout, the primary suspension will be at compression y_M due to the weight of the vehicle.

At time $t = 0$, the wheel "jumps" off the supporting rail with a horizontal velocity u. From this point on, the forces acting on the wheel are the gravitational $(M+m)\,g$ and the spring reaction $k\,(y-y_M)$. This way, the planar motion of the wheel is composed by two independent components as portrayed in Fig. 5: a non-accelerating motion in the horizontal direction (3), and an oscillatory motion in the vertical direction (4) (the damping ratio ξ of the primary suspension is neglected).

$$x = ut \tag{3}$$

$$y = \frac{(M+m)g}{k}[1 - \cos(\omega t)] \tag{4}$$

The orbit of the wheel is computed by eliminating time in the equations of motion. Considering an idealised (planar) surface for the rail, the displacement vector of the impact point (x_i, y_i) is the solution of the following system:

$$y = \frac{(M+m)g}{k}\left[1 - \cos\left(\omega\frac{x}{u}\right)\right] \tag{5}$$

$$y = d - \frac{d}{b}x \tag{6}$$

where d is a function of wheel wear w and rail wear w_R, as well as of the extent of the flangeway gap g, and b is the length of the ramp. For a given horizontal train velocity u, the point at which the main impact will occur can be back-estimated numerically.

The impact velocity of the wheel comprises the normal components of the horizontal (u_n) and vertical (v_n) velocity of the wheel at impact, computed according to the following formulae:

$$u_n = u_o \sin \beta \cong u_o \beta \tag{7}$$

$$v_n = v \cos \beta \cong v \tag{8}$$

where β is the inclination angle of the plane (i.e., the ramp).

Hence, the impact velocity of the wheel can be computed as:

$$V_{\text{impact}} = u_o \beta + v \tag{9}$$

The above expression of the impact velocity is used to estimate the loading to the track for the 3-D finite element analysis. This way, the loading is an impact velocity and not a contact force, allowing for the system to dynamically respond naturally.

Based on the loading description described above, a time domain simulation is performed. The computation time required for a run of duration 0.1 s is approximately 0.5 h on a last generation PC-type processing unit.

3. Comparison of model results and validation

To assess the accuracy and reliability of the two methods, numerical results are compared with line measurements on different turnout systems, all taken from urban railway networks. Three such comparisons are presented herein:

i. A turnout with vignole type rail, from the RATP underground network in Paris, negotiated at speeds up to 55 km/h by a trainset formed by four-axle coaches with bogies;
ii. A turnout with grooved type rail, from the STIB tramway network in Brussels, tested under the passage of an articulated trainset at the maximum speed of 15 km/h;
iii. A turnout with grooved rail and "flange bearing" crossing, from the tramway network of De Lijn in Antwerp, tested under the passage of an articulated trainset at the maximum speed of 20 km/h.

In all three cases, we consider a train negotiating the turnout along the main track: line measurements clearly showed that this is the situation leading to the highest impact effects, due to the train travelling at a higher speed.

Among the available measurement points, rail acceleration on the frog nose is taken as the most representative for comparison of the two methods with field data. Fig. 6 compares the $\frac{1}{3}$ octave band levels of vertical rail acceleration measured at the crossing nose for the three validation cases. Due to the substantially larger train speed (compared to the other two cases) and to the poor geometric condition of the turnout at the time of measurement, the RATP metro turnout shows the highest levels of track vibration. On the other hand, the STIB turnout shows the lowest vibration levels: a difference of 30 dB or more compared to the RATP turnout. Besides from the aforementioned attributes (train velocity and geometric conditions), this very large difference can also be attributed to the lower axle load of the vehicle used in the tests. The De Lijn case sets approximately mid-way between RATP and STIB, in terms of levels of turnout vibration: the higher excitation with respect to the STIB case is mainly due to the slightly higher speed, but is especially associated with the use of a "flange bearing" crossing type.

In conclusion, the three validation cases can be considered altogether representative of a wide range of train–turnout interaction conditions in urban rails, as they cover different levels of excitation, different types of rail profile and crossing concept (with gap/flange bearing) and different stages of turnout geometry degradation produced by service.

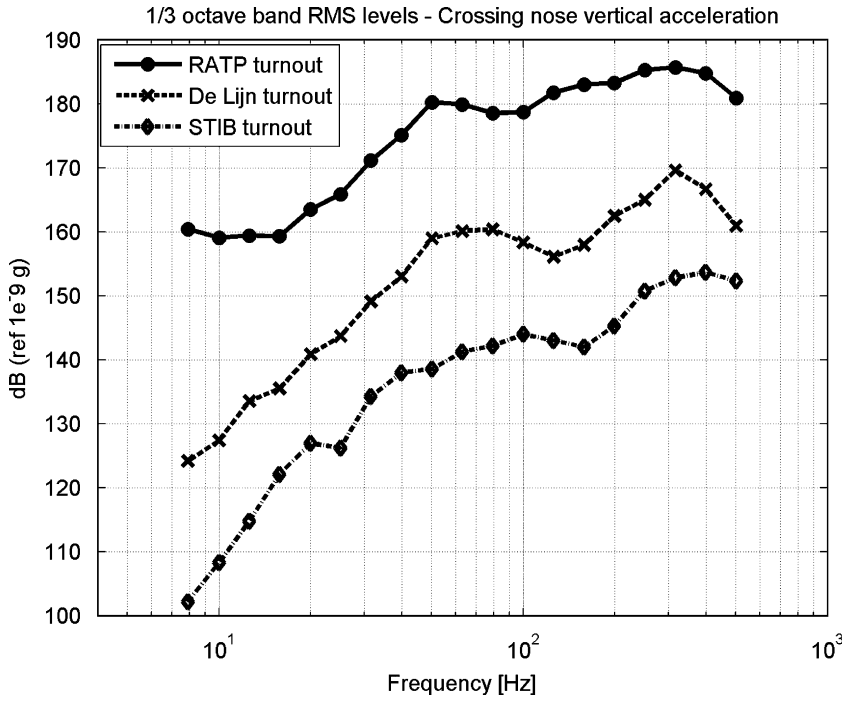

Fig. 6. Comparison of the vertical acceleration levels on the crossing nose for the three measured turnouts (1/3 octave band representation).

3.1. The RATP turnout case

At the RATP site, measurements were performed by running a test train composed by five 4-axle vehicles (axle load 78.5 kN) on a vignole rail turnout. On the track side, vertical and lateral rail acceleration was measured in the centre of the crossing panel and on a section of standard track. On the train side, the vertical axlebox and bogie frame accelerations were measured on one bogie, and additionally car body acceleration was measured. Care was spent in ensuring a stiff mounting of the accelerometers on the measuring points, to avoid "mechanical filtering" effect at high frequency. All data were low-pass filtered at 2.5 kHz and sampled at 6 kHz.

Train passages along the main and branching line were recorded at speeds ranging from 25 to 55 km/h. Additionally, track inertance measurements in vertical and lateral direction were taken using impulsive excitation, in the same locations where rail acceleration was measured. Track inertance measurements were used to identify the parameters of the finite element models defined for the turnout.

For the sake of conciseness, the comparison is focused here on rail acceleration, considering the centre of the crossing. The comparison is also confined to the vertical component of rail acceleration, since Method B does not consider the horizontal component of track excitation.

The measured and simulated time history of the vertical rail acceleration at the crossing nose of the RATP turnout during train passage at 55 km/h is compared in Fig. 7. All signals are low pass filtered at 500 Hz, to confine the comparison within the frequency range of validity assumed for Method A, which is restricted by the simplifying assumptions introduced in the turnout model, and in particular by the use of beam elements to represent the rails. The comparison is performed over a time duration of 0.1 s, centred over the passage of a wheel on the crossing nose.

In the experimental acceleration record, the level of acceleration peaks corresponding to the passage of different wheelsets present some differences, which are explained by differences in the state of wheel surfaces and possibly also by the different condition of primary suspensions in the bogies. In simulation results obtained from Method A, more limited differences between the peaks associated to different wheelsets are

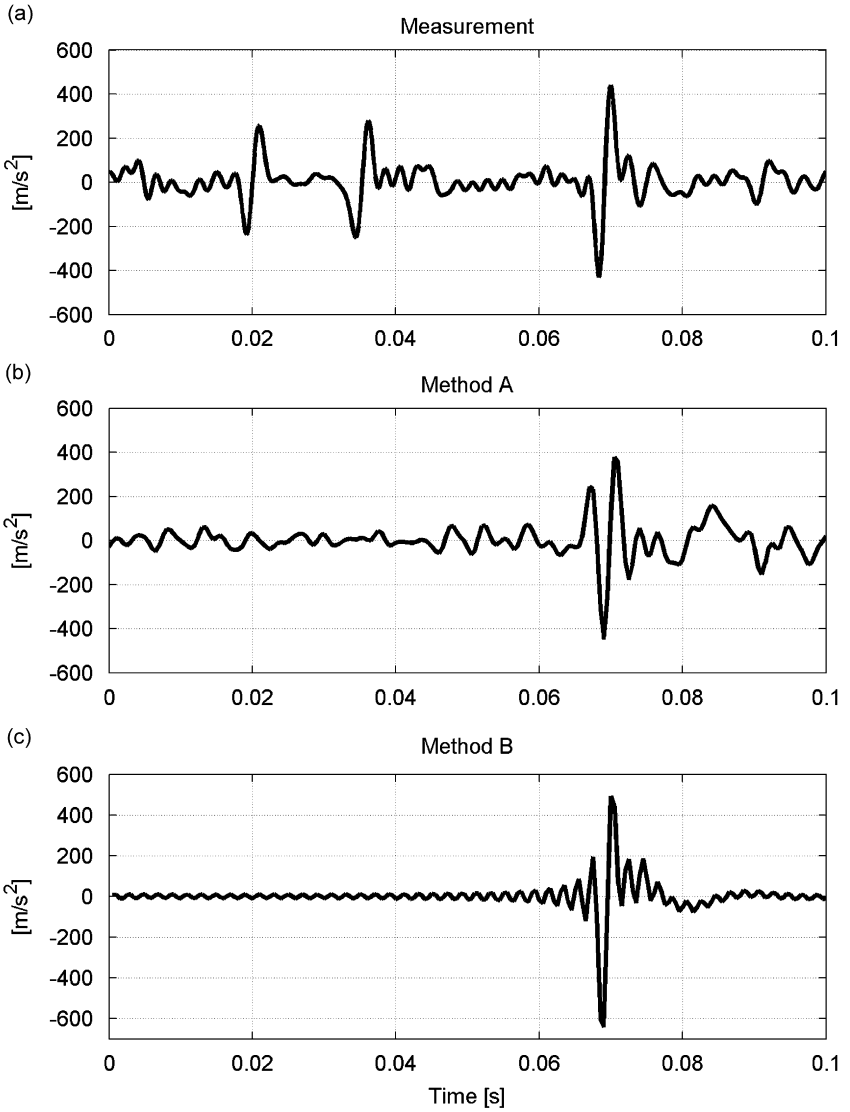

Fig. 7. Comparison between line measurements at the RATP reference turnout and simulation results—vertical acceleration at the crossing nose: (a) line measurement, (b) Method A, and (c) Method B.

observed, since the same level of irregularity was assumed for all wheels and the same model was used for all primary suspensions in the trainset. Still, a difference is observed between the leading bogie in the trainset (which travels over an "unperturbed" turnout geometry), and the other bogies. Finally, Method B considers the passage of one single wheelset, and therefore produces one single peak of acceleration. In Fig. 7, the wheel passage producing the highest acceleration peak was selected both in the measured data and in the results from Method A, to be compared with the single peak produced by Method B.

In the measured record, the main acceleration pulse, presumably corresponding to the wheel being transferred from the closure rail to the crossing nose, is preceded by two pulses of lower amplitude. The main pulse is rather symmetric, in the sense that its positive and negative extreme values are almost equal in absolute value. The rest of the acceleration pulses are probably produced by concentrated irregularities on the railhead, before and after the frog nose. Those were verified through visual inspection of the turnout during the measurements. Finally, a non negligible level of random excitation is observed over the whole considered

Table 1
Comparison of peak and rms values of vertical crossing nose acceleration for the RATP turnout.

	Measurement (m/s^2)	Method A (m/s^2)	Measurement vs. Method A (dB)	Method B (m/s^2)	Measurement vs. Method B (dB)
Positive max. amplitude	440	378	−1.3	493	1
Negative max. amplitude	430	447	0.3	640	3.5
rms	83	79	−0.4	86	0.3

duration of the signal, representing the effect of wide band random irregularities of the rails due to wear, alignment errors etc.

Figs. 7b and c depict the time histories of the frog vertical acceleration, as obtained from numerical simulations performed using the Methods A and B, respectively. In both cases, the side pulses due to concentrated defects are not present, since the effect of concentrated railhead irregularities was not considered in either of the simulations due to lack of information about the actual geometry of the railhead along the switch. The result of Method A shows a main pulse during the passage over the crossing nose, with a shape similar to the measured, and with positive and negative extreme values in agreement with the measurements. The effect of rail irregularities producing a random forcing effect also appears to be correctly reproduced by Method A, which predicts an amplitude of random vibration in the range of $\pm 80\,m/s^2$, also in agreement with the measurements (Fig. 6a). Method B also predicts correctly the main vertical acceleration pulse, which corresponds to the impact of the wheel onto the crossing nose. The pulse is slightly asymmetric, with the negative maximum amplitude being larger than the positive, but the overall levels of vibration are in line with the measurements.

Table 1 compares the maximum and rms values obtained through line measurements with the numerical predictions. For both methods, the deviations with respect to the measured values are in the range of ± 1 dB. The only exception lies in the negative peak value predicted with Method B, which is overestimated compared to the measurement by 3.5 dB. The overall comparison can be seen as quite satisfactory, since the two models are in good agreement with each other and with the measurements.

Method A is used to investigate how the energy of vibration is distributed over the whole frequency range of interest. Since Method B focuses on the main impact (occurring at the crossing nose), neglecting the effect of random track irregularities, it would not be meaningful to be used for this kind of comparison. The numerical prediction (using Method A) is compared to the measurements in terms of $\frac{1}{3}$ octave band levels of vertical rail vibration at the crossing nose (Fig. 8). Since one of the main goals of the *TURNOUTS* project was to achieve a modelling accuracy of ± 3 dB, in this comparison we also plot the associated "tolerance band" (with a dotted line). The numerical prediction clearly falls within the ± 3 dB tolerance band almost throughout the whole frequency range of interest. Taking into account that the measurements were conducted in the field (i.e., on an existing turnout under real traffic), and not under well defined laboratory conditions, this can be seen as a very good result for the degree of uncertainties involved. The only noticeable discrepancy between measurement and simulation is observed at 126 Hz. This is attributed to an anti-resonance of the turnout finite element model, which was not observed in experimental inertance measurements.

In conclusion, both methods predict accurately the total rms value of rail vibration on the crossing nose, while Method A also reproduces successfully the distribution of the energy of vibration over the frequency range of interest (0–500 Hz).

3.2. The STIB turnout case

The second case used for validation refers to the case of a grooved rail turnout from the tramway network of STIB in Brussels, negotiated at 15 km/h speed by a 6-axle articulated tramcar having axle load of 48 kN. As in the RATP site, vertical and lateral rail acceleration was measured in the centre of the crossing panel.

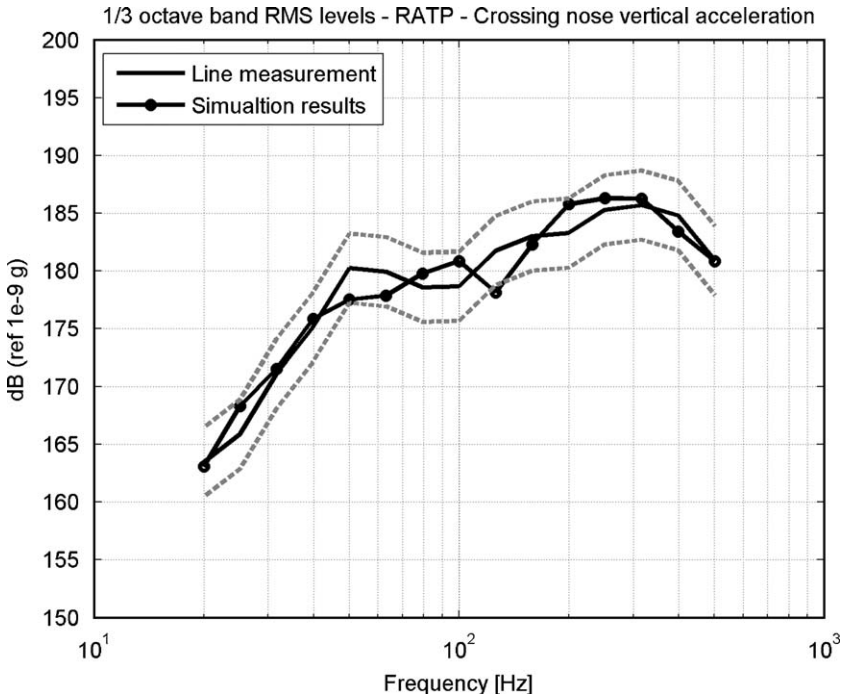

Fig. 8. Comparison between line measurements at the RATP reference turnout and simulation results (Method A): vertical crossing nose acceleration for complete train negotiation ($\frac{1}{3}$ octave band representation).

The measured signals were low-pass filtered at 2.5 kHz and sampled at 6 kHz. Also in this case, the vertical and lateral track inertances were measured and used to identify the parameters of the finite element models used for numerical simulations presented in this section.

Fig. 9a reports the time history of the measured vertical acceleration of the crossing nose, after low-pass filtering with a cut-off frequency of 500 Hz. With respect to the RATP case, the levels of vertical vibration produced by train passage are almost two orders of magnitude lower, and the impact effect produced by wheel passage, although well recognisable, is less predominant compared to the random effect produced by track irregularities. This is mainly due to the better geometric condition of the turnout, which was in this case a newly installed one.

The numerical prediction using Method A is shown in Fig. 9b: the model reproduces the superposition of the random vibration produced by rail irregularities with the peak acceleration pulse produced by wheel passage over the crossing nose. The positive extreme and rms values provided by this modelling approach are very well in line with the measured values (see also Table 2) whereas the negative extreme value is underestimated. This discrepancy could be due to the fact that track irregularity on the turnout was not measured, and hence reasonable assumptions (but not necessarily in full compliance with reality) had to be made on this input of the model.

The numerical prediction using Method B is shown in Fig. 9c. Observe that the computed vertical acceleration pulse is somehow different form the measured response. This is mainly due to the fact that rail irregularities are not accounted for in this approach. However, the extreme and rms values are in very good agreement with the measurement (see also Table 2). It is important to point out that in the case of Method B, which also takes into account soil–foundation interaction effects, soil resilience proved to be a key parameter with regard to the peak values of rail acceleration, and related frequencies. The results reported herein refer to a soil bedding modulus of 500 MN/m^3. This constitutes a reasonable assumption for the soil conditions at the STIB site, but not necessarily in full compliance with reality (no such measurement was conducted).

As for the RATP case, Fig. 10 compares line measurements with numerical results (using Method A) in terms of $\frac{1}{3}$ octave band representation of the vertical rail vibration at the crossing nose, considering the passage

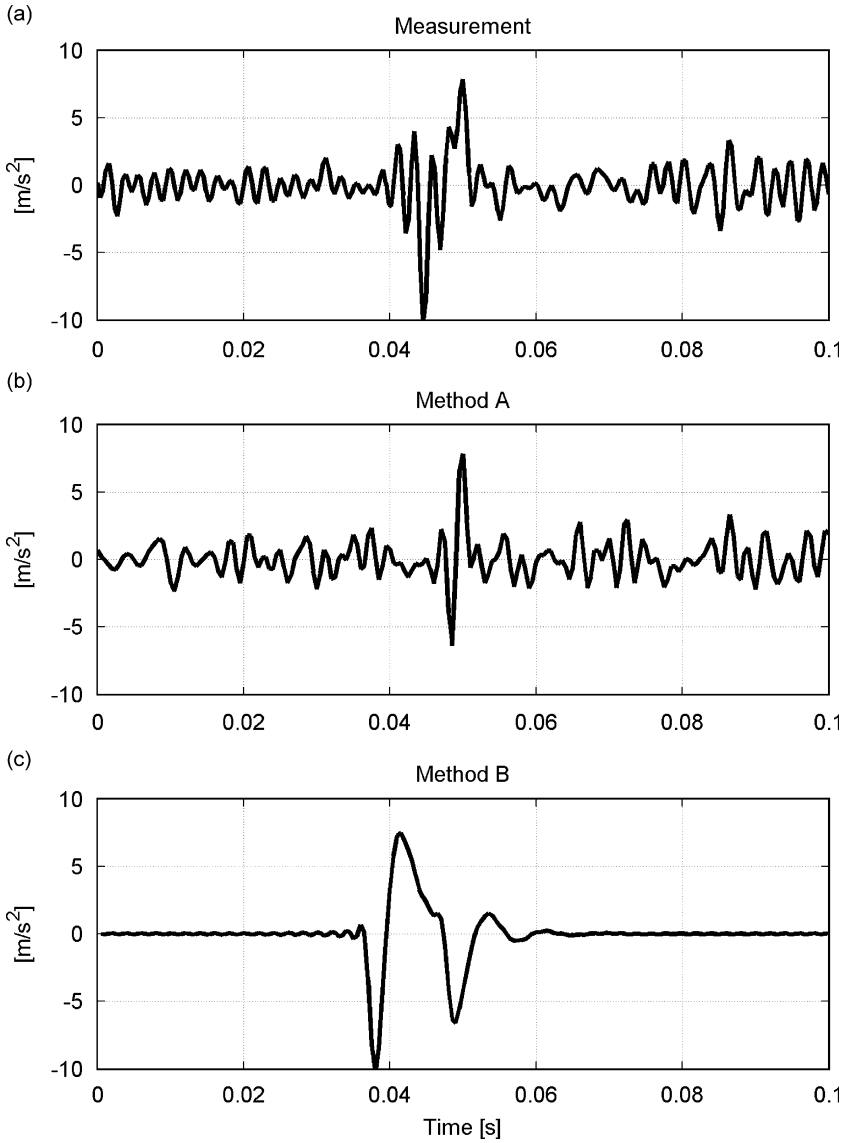

Fig. 9. Comparison between line measurements at the STIB turnout and simulation results—vertical acceleration at the crossing nose: (a) line measurement, (b) Method A and (c) Method B.

Table 2
Comparison of peak and rms values of vertical crossing nose acceleration for the STIB turnout.

	Measurement (m/s^2)	Method A (m/s^2)	Measurement vs. Method A (dB)	Method B (m/s^2)	Measurement vs. Method B (dB)
Positive max. amplitude	7.9	7.8	−0.1	7.5	−0.5
Negative max. amplitude	10.6	6.4	−4.3	10.4	−0.2
rms	1.76	1.45	−1.6	1.70	−0.3

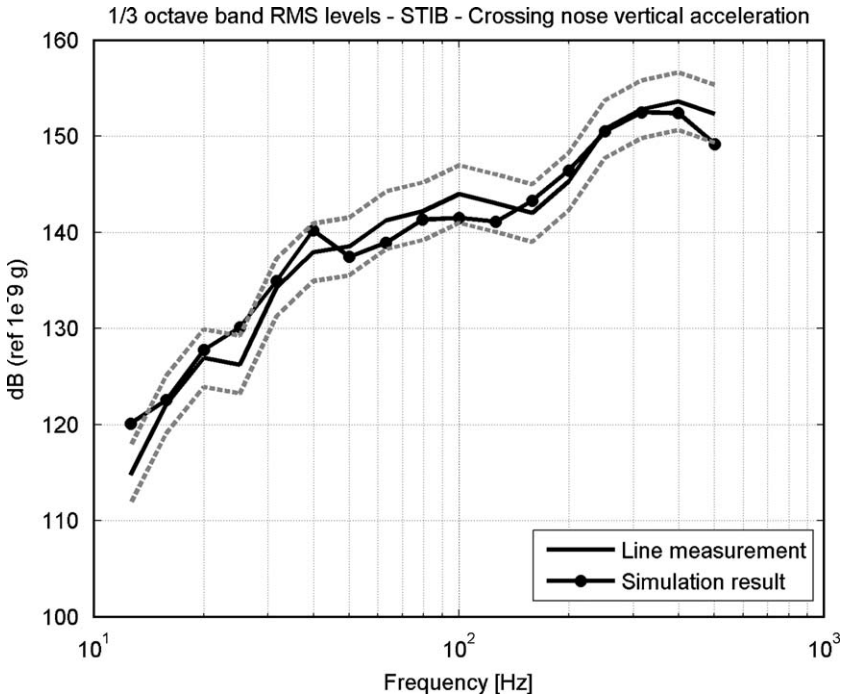

Fig. 10. Comparison between line measurements at the STIB turnout and simulation results (Method A): vertical crossing nose acceleration for complete train negotiation ($\frac{1}{3}$ octave band representation).

of the entire trainset. Although the vibration levels are totally different from the RATP case, the results are again in good agreement with the measurements, with the deviations always remaining in the ± 3 dB range.

3.3. The De Lijn turnout case

The last comparison also deals with a grooved rail turnout, in this case from the De Lijn tramway network in Antwerp. Despite the similarity with STIB, this case is substantially different in terms of axle loads (72 kN/axle in this case) and train passage velocity (20 km/h instead of 15 km/h in STIB). In addition, the De Lijn crossing panel is designed according to the "flange bearing" concept, i.e., the passage of the wheel along the crossing panel is realised by gradually decreasing the depth of the rail groove, until contact takes place between the outer surface of the wheel flange and the bottom of the rail groove, so that the wheel tread is then lifted until completion of the passage over the crossing. This way, the large impact on the crossing nose is avoided, replaced by two smaller impacts, produced when the contact is transferred from the wheel tread to the flange tape and when tread contact is restored after the passage of the crossing.

Measured quantities again consisted in the vertical and lateral acceleration of the crossing panel. With respect to the measurements taken at RATP and STIB in this case 13 measuring points were taken in different positions of the crossing panel. Direct and cross inertances of the crossing panel were measured in these locations, using impact excitation applied in the centre of the panel, and these data were used to calibrate the finite element model of the turnout.

Fig. 11a illustrates the time history of the vertical rail acceleration measured at the centre of the crossing. Compared to STIB, the levels of vibration are approximately one order of magnitude higher. The simulation performed using Method A (Fig. 10b), shows that the single large impact obtained on crossings presenting a gap (like the RATP and the STIB ones) is replaced by a sequence of impulses corresponding to the sudden transition of contact from the wheel tread to the flange tape and then back to the tread. This is consistent with the shape of the measured acceleration time history, showing that the model is able to capture the peculiar

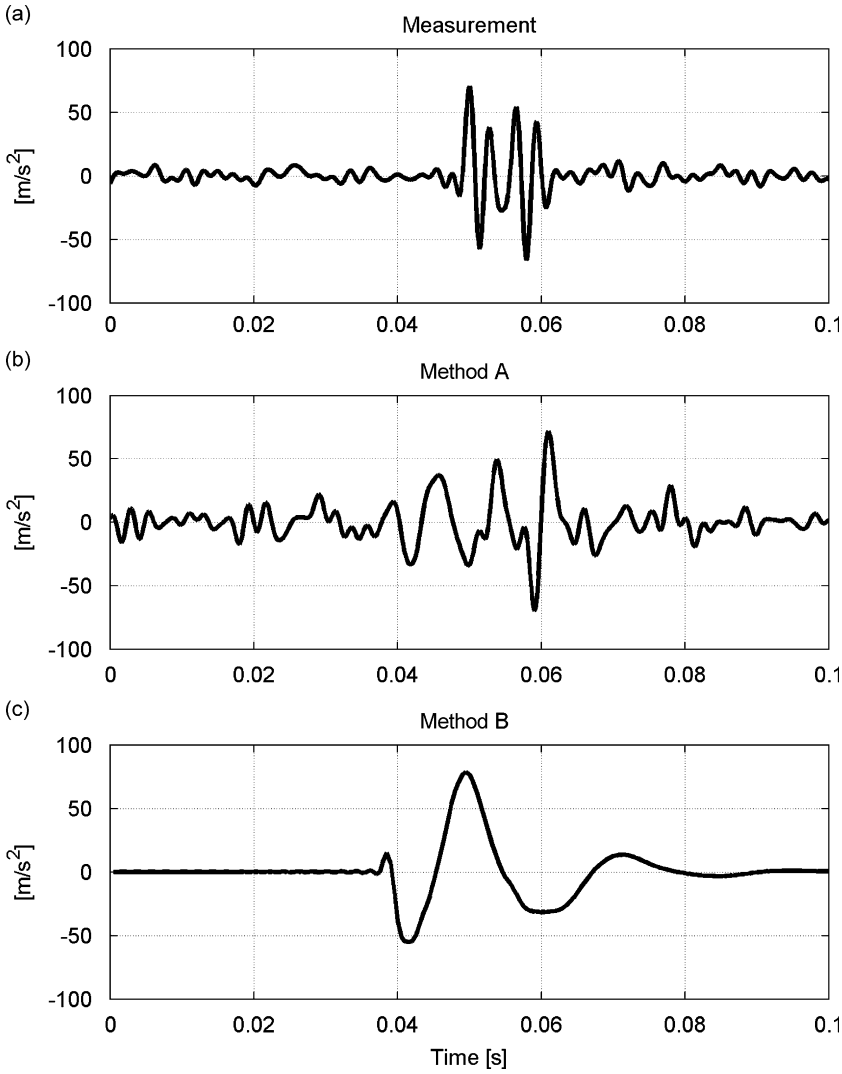

Fig. 11. Comparison between line measurements at the De Lijn turnout and simulation results—vertical acceleration at the crossing nose: (a) line measurement, (b) Method A and (c) Method B.

Table 3
Comparison of peak and rms values of vertical crossing nose acceleration for the De Lijn turnout.

	Measurement (m/s^2)	Method A (m/s^2)	Measurement vs. Method A (dB)	Method B (m/s^2)	Measurement vs. Method B (dB)
Positive max. amplitude	70.3	71.8	0.2	60.8	−1.3
Negative max. amplitude	66.2	69.8	0.5	60.8	−0.7
rms	13.0	16.2	1.9	13.6	0.4

type of impact excitation which is produced in this type of turnout. Furthermore, the maximum and rms values of the acceleration are very close to the measured, as summarised in Table 3.

The simulation result using Method B is depicted in Fig. 11c. In contrast to Method A, this approach intrinsically allows simulating of one single impact of the wheel on the turnout, and the result reported herein

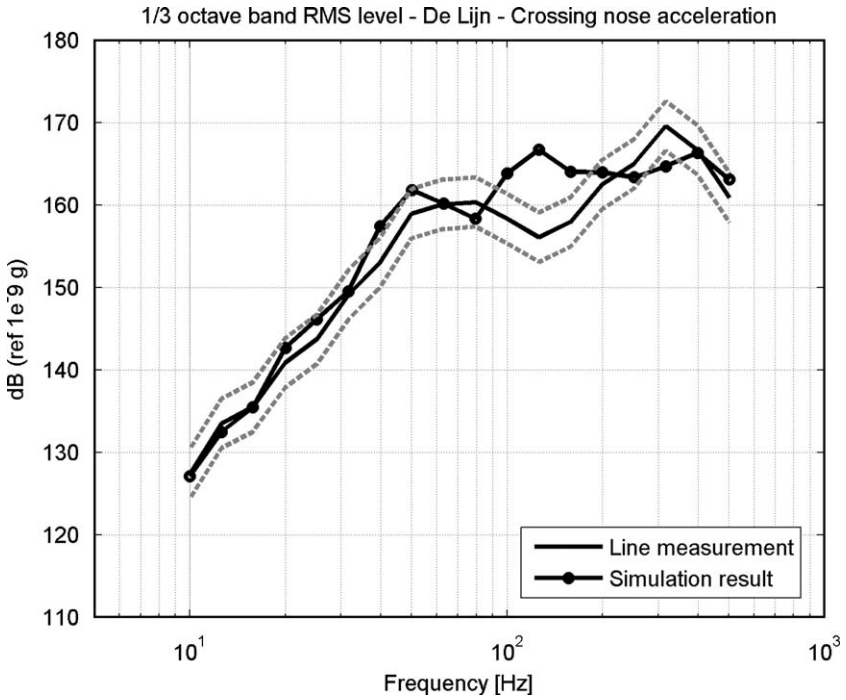

Fig. 12. Comparison between line measurements at the De Lijn turnout and simulation results (Method A): vertical crossing nose acceleration for complete train negotiation ($\frac{1}{3}$ octave band representation).

refers to the impact of the outer flange surface on the bottom of the rail groove, that takes place during the entrance of the wheel into the crossing panel. The extreme values obtained in this way are in very good agreement with the measured ones, although the duration of the acceleration pulse is quite different, so that the frequency content of this simulation is not the same as in the measurements.

Fig. 12 compares measured and simulated vertical rail accelerations (using Method A) for the passage of the complete trainset using a $\frac{1}{3}$ octave band level representation. The numerical result generally lies well within the ± 3 dB tolerance band, with the only exception being the 100–160 Hz frequency range. This difference is due to a difference between the actual track inertance (that was measured in situ by impact tests) and the inertance of the track finite element model used in the simulation. In this frequency range, although several calibration attempts were conducted, it was not possible to obtain a better "fit" between numerical end experimental frequency response function. Despite this discrepancy, the overall vibration pattern with respect to frequency is well reproduced by the model, and the result of the comparison can still be considered satisfactory.

4. Sensitivity analysis

Having validated the developed numerical models against a variety of turnout systems, we proceed in a parametric sensitivity analysis of the main parameters affecting dynamic turnout performance. The results of this parametric investigation were used within the *TURNOUTS* project to design and fine-tune new turnout concepts for low vibration and noise transmission in urban turnout systems [9]. This section summarises the main results and conclusions of the sensitivity analysis, with respect to a vignole rail turnout, such as the RATP turnout. Measurements and calculations on this turnout showed that the vibration levels may increase substantially in presence of a degraded geometry, mainly due to the effect of wear in combination with the relatively high (for an urban rail system) train speed. Hence, besides from the mechanical properties (stiffness and damping) and the standard irregularities of the track, the sensitivity analysis also deals with the quality of rail/track geometry. Table 4 summarises the test cases considered in the parametric analysis.

Table 4
List of cases considered in the sensitivity analysis for the vignole rail type turnout.

Test case	Description	Rail profile	Track irregularity	Parameters of the upper resilient layer (per sleeper)		Parameters of the lower resilient layer (per sleeper)	
				Stiffness (MN/m)	Damping factor at 50 Hz	Stiffness (MN/m)	Damping factor at 50 Hz
V1	Reference	Worn	Bad quality	200	0.05	100	0.05
V2	Profile correction (PC)	Corrected	Bad quality	200	0.05	100	0.05
V3	Track geometry correction (TC)	Worn	Good quality	200	0.05	100	0.05
V4	Profile and track geometry correction (PC + TC)	Corrected	Good quality	200	0.05	100	0.05
V5	Ballast mat (BM)	Worn	Bad quality	200	0.05	60	0.30
V6	Under sleeper pad (USP)	Worn	Bad quality	70	0.30	100	0.05
V7	Ballast mat and under sleeper pad (BM + USP)	Worn	Bad quality	70	0.30	60	0.30
V8	Profile correction, ballast mat and under sleeper pad (PC + BM + USP)	Corrected	Bad quality	70	0.30	60	0.30
V9	Profile and track geometry correction ballast mat and under sleeper pad (PC + TC + BM + USP)	Corrected	Good quality	70	0.30	60	0.30

With respect to the rail profile, two alternatives were considered: (a) the actual "worn" rail profile, as obtained from the aforementioned comparisons with measurements on the RATP turnout; (b) a "corrected" rail profile, which corresponds to an improved rail geometry (achievable through maintenance operations that restore the original idealised track geometry), providing a 75% reduction of vertical wheel displacement (and of the associated impact velocity, see also Fig. 5) during wheel passage over the nose of the crossing.

Two levels of track irregularity were also considered in the parametric analysis: (i) "bad quality", corresponding to the level of irregularity specified by ORE as "high" [17]; and (ii) "good quality", in which the level of irregularity is 5 times lower.

With respect to track resilience, the values identified for the RATP turnout on the basis of the previously discussed comparisons were assumed as the reference, representative of a standard ballasted track. In addition to the standard track, two possible improvements were considered:

- introduction of a ballast mat (BM), separating the ballast from the underlying soil;
- introduction of an under-sleeper pad (USP), placed between the sleeper and the ballast.

Considering the change of one parameter at a time and some combinations where more than one parameter is varied, a total of nine cases were obtained for parametric analysis. All these cases were simulated with the vehicle negotiating the turnout at 55 km/h, corresponding to the maximum speed adopted in the test runs performed on the RATP turnout.

To evaluate the effectiveness of the different design alternatives, and to derive the optimum combination of track parameters, the following measures are used as indicative of turnout performance:

(1) Vertical rail acceleration on the crossing nose: it is representative of track vibration levels, and directly associated with the distress of turnout components;
(2) Vertical soil acceleration under the crossing nose: it is representative of the level of vibration transmitted to the environment, and hence directly associated with the nuisance levels due to the presence of the turnout;
(3) Wheel–rail contact force during train passage over the crossing panel (vertical component, first wheelset in the trainset): to quantify train–track interaction effects.

4.1. The effect of rail profile and track geometry correction

Fig. 13 illustrates the effect of rail profile and track geometry correction with respect to rail and soil accelerations, in terms of $\frac{1}{3}$ octave band levels (Ref. 1e-9 g). As shown in Fig. 13a, the correction of rail profile (i.e., a marked reduction of the wheel lift-and-sink motion during passage over the crossing nose, case V2) provides a substantial reduction of impact effects, resulting to a decrease of rail vibration of the order of 5 dB or more at frequencies below 300 Hz, and 2–3 dB at higher frequencies. The rms of rail vibration are compared in Table 5: rail profile correction reduces the rms rail vibration by 5.7 dB. In stark contrast, a correction of track geometry (case V3) has almost no effect on the crossing nose accelerations: to explain this finding, it should be considered that impacts on the crossing nose are caused by the sudden vertical displacements of the wheel occurring when this body is transferred from the stock rail to the crossing nose: this effect is mostly associated with the rail profile, and is only marginally affected by track geometry. Correspondingly, the combined effect of rail profile and track geometry correction (case V4) does not bring any sensible advantage with respect to profile correction only.

As far as soil vibration is concerned, Fig. 13b shows that the effect of rail profile correction is beneficial in the frequency range up to 50 Hz, leading to a reduction of about 10 dB in soil vibration. However, for higher frequencies the benefit is not as pronounced, becoming practically negligible above 100 Hz. Since most part of the energy of soil vibration lies in this higher frequency range, the reduction of soil acceleration in terms of rms value is 3.4 dB (see Table 5). As it would be expected, the correction of track geometry (case V3 against V1 and case V4 against V2) has a very limited effect on soil vibration levels.

Table 5 also reports the rms of the vertical acceleration in the centre of the sleeper laying below the crossing nose and for the ballast degree of freedom below that sleeper. Considering the reference case V1, the abatement of vibration from the rail to the sleeper is 3.5 dB, from the sleeper to ballast it is 8.3 dB and from ballast to soil is 14.7 dB. Similar values of vibration abatement between the different track layers are found also introducing profile correction, case V2, although the reduction of vibration from the sleeper to the ballast dof is in this case 5.9 dB, which is lower than the value obtained in the reference case.

Fig. 14 shows the time history of the vertical contact force on the wheel travelling over the crossing nose (leading wheelset in the trainset). In the figure, the results obtained for cases V1, V2 and V3 are shown, whereas the result of case V4 is not shown for the sake of brevity, but presents minor differences with respect to the result of case V2. With reference to the same quantity, the maximum wheel loading and unloading is summarised in Table 5: the maximum wheel loading factor is obtained as the ratio between the maximum value of the force and the wheel static load, whereas the maximum wheel unloading is defined as the ratio between the minimum value of the vertical contact force and the static wheel load. In case of loss of contact, the minimum contact force becomes zero and the unloading coefficient reaches the upper bound of 100%. Evidently, rail profile correction (cases V2 and V4) provides the best results: in the reference case, corresponding to highly worn rail geometry, the wheel looses contact with the rail (100% wheel unloading) due to the degraded condition of the crossing nose surface. Before and after the loss of contact, important amplification of the wheel–rail contact force takes place, so that the maximum vertical load on the wheel is nearly 3 times the static value, producing strong rail vibration. With the improvement of rail profile geometry only (case V2), contact loss is avoided, and maximum wheel loading is reduced drastically, leading to a much more favourable train–track interaction condition. On the other hand, the reduction of track irregularity only (case V3) provides only a minor reduction in the dynamic force amplification, and does not prevent the loss of contact between the wheel and the rail. Finally, the combined use of rail profile and track geometry correction does not provide further advantage with respect to profile correction only.

4.2. The effect of track resilience

Fig. 15 illustrates the effect of track resilience on rail and soil vertical accelerations. The introduction of a BM (case V5), has a limited effect on rail vibration: a slight reduction by 1–2 dB is observed in the 30–60 Hz frequency range, which is the result of increased damping provided by the BM (elastomeric material); in contrast, an increase is observed at 125 Hz, due to the fact that the track anti-resonance originally present in that frequency range disappears after introduction of the ballast mat. Hence, the rms value of rail acceleration

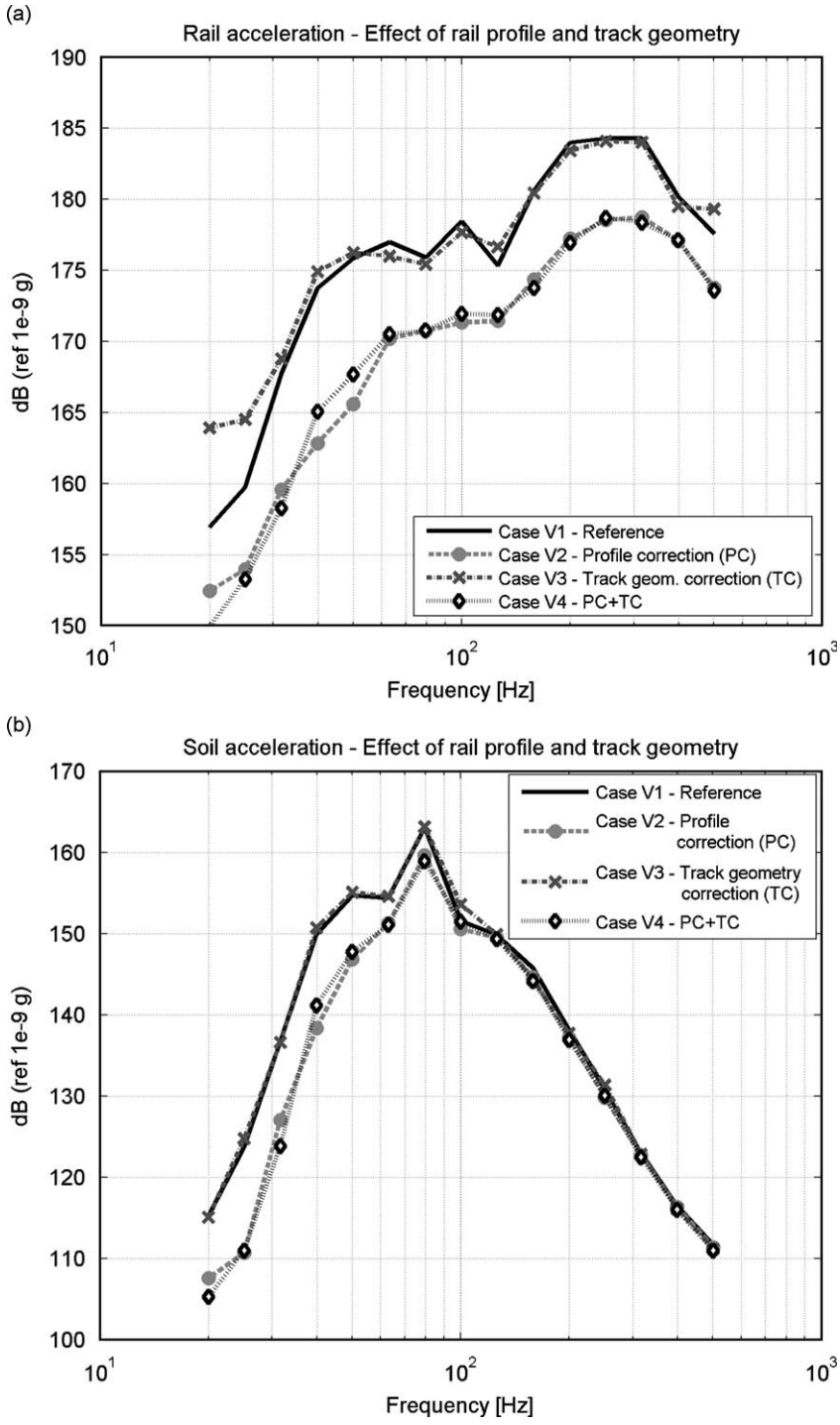

Fig. 13. The effect of rail profile correction and track geometry correction on the $\frac{1}{3}$ octave band levels of vertical rail acceleration (a) and vertical soil acceleration (b).

is close to the reference case V1 (Table 5). Introduction of an USP (case V6) leads to a slight decrease of rail vibrations in the low frequency range; above 125 Hz a reduction of the order of 1–4 dB is observed. This effect is again produced by the increase of track damping provided by the USP: compared to the use of a ballast mat,

Table 5
The effect of rail and track geometry: comparison of peak and rms values for rail and soil accelerations.

	Vertical acceleration rms (m/s^2)				Vertical contact forces	
	Rail	Sleeper	Ballast	Soil	Max wheel loading. (%)	Max. wheel unloading (%)
Case V1	36.5	24.2	9.33	1.72	36.5	100.0
Case V2	19.0	13.0	6.57	1.16	19.0	49.7
Case V3	35.9	24.1	9.29	1.78	35.9	100.0
Case V4	18.8	13.0	6.34	1.11	18.8	51.5
Case V5	34.5	23.2	7.69	1.06	34.5	100.0
Case V6	30.6	23.5	6.01	1.13	30.6	100.0
Case V7	30.5	22.2	5.67	0.79	30.5	100.0
Case V8	15.3	10.8	3.24	0.56	15.3	45.7
Case V9	15.3	11.0	3.21	0.55	15.3	45.4

Reduction of rms acceleration with respect to case V1.

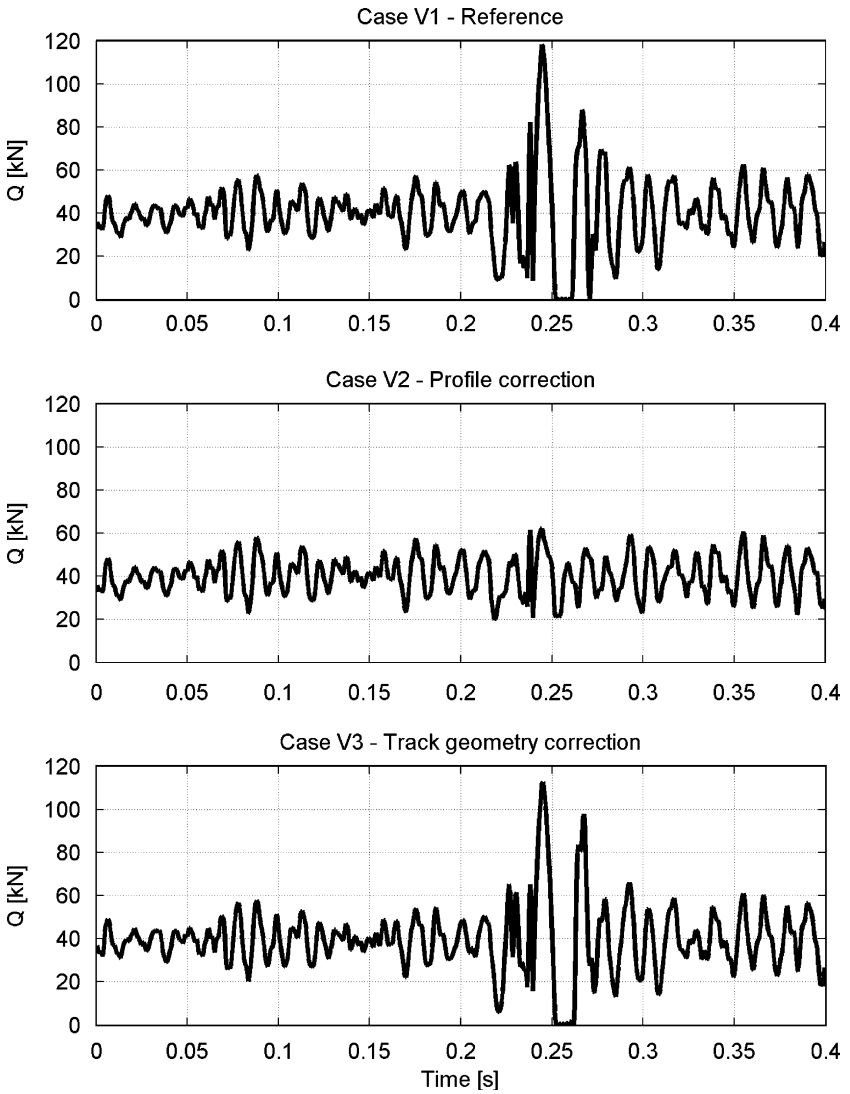

Fig. 14. The effect of rail profile correction and track geometry correction on the time history of the vertical wheel/rail contact force.

in this case the elastomeric layer is added closer to the rail level, turning out to be more effective in reducing rail vibration in the high-frequency range. In terms of rms and extreme values of rail acceleration, the effect of the USP is a reduction of 1.5 dB (see Table 5). When the combined introduction of BM and USP is considered (case V7), the level of rail vibration is slightly increased with respect to the reference case in the frequency

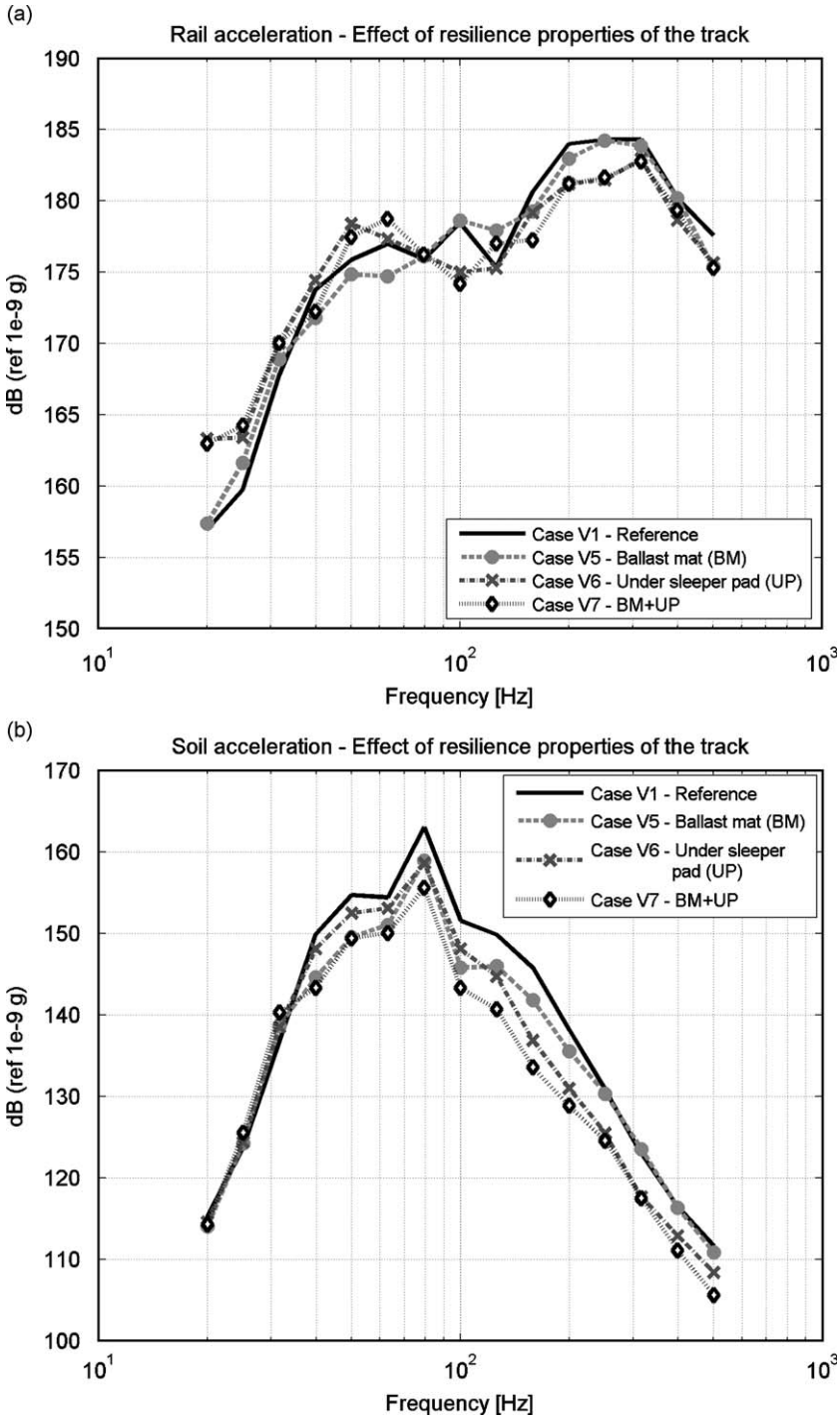

Fig. 15. The effect of track resilience modifications on the $\frac{1}{3}$ octave band levels of vertical rail acceleration (a) and vertical soil acceleration (b).

range 50–80 Hz, and is slightly decreased at higher frequencies; the overall rms value is in this case almost the same as the one obtained using USP only.

The effect of track resilience on soil vibration is shown in Fig. 15b. Using a ballast mat, soil vibration levels are reduced substantially: 2–5 dB in the frequency range 40–200 Hz, and the overall reduction of the rms soil

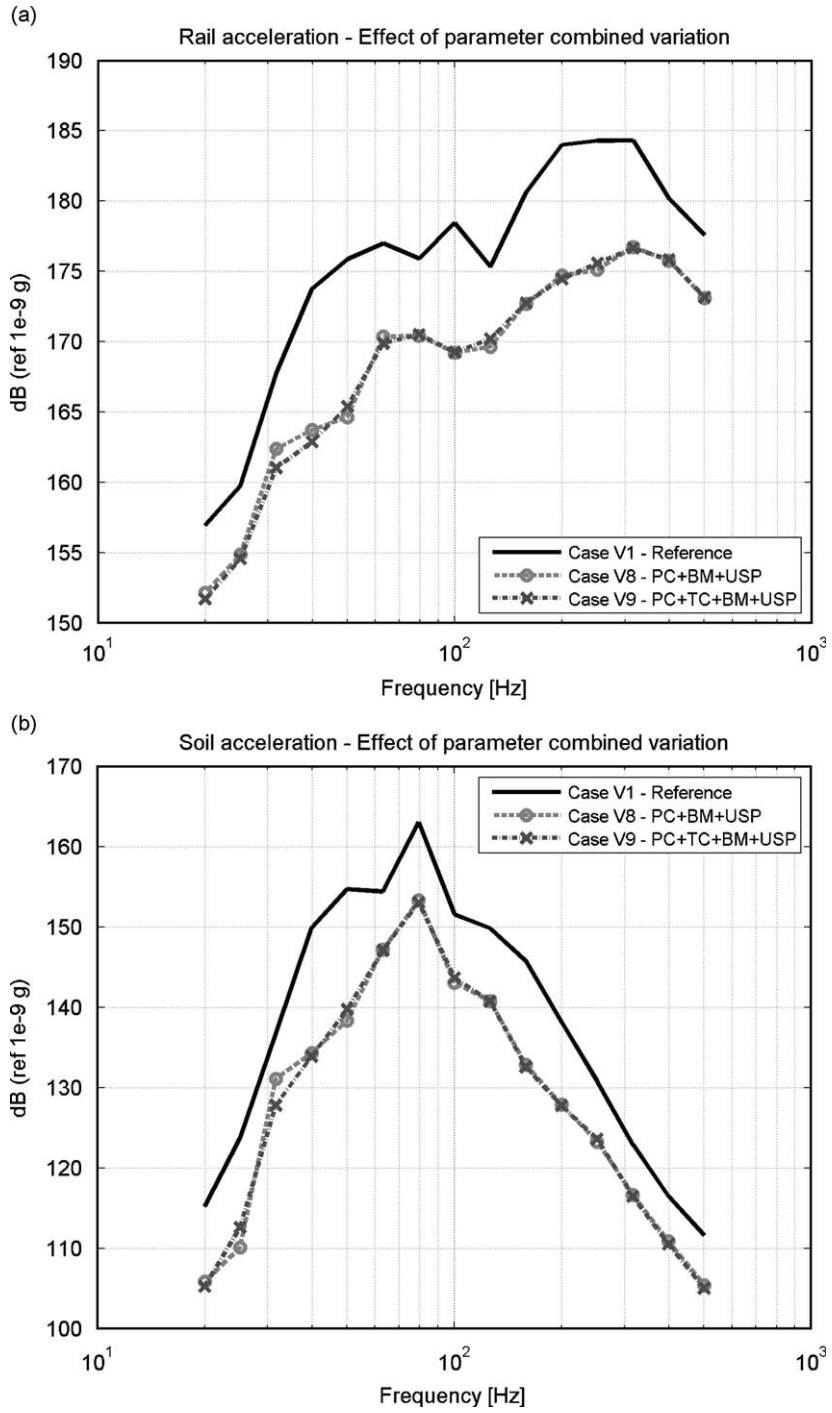

Fig. 16. The combined effect of geometric corrections and track resilience modifications on the $\frac{1}{3}$ octave band levels of vertical rail acceleration (a) and vertical soil acceleration (b).

vibration is rather remarkable (around 4.2 dB). This beneficial effect is mainly due to the decrease of track foundation stiffness, which provides a higher effect of vibration filtering from the ballast to the soil. This is confirmed by the levels of acceleration obtained in the sleeper and in the ballast, reported in Table 5: the level of sleeper vibration is barely affected, but vibration abatement from the sleeper to the ballast is increased substantially. Using an USP, the reduction of soil vibration with respect to case V1 is lower below 100 Hz, but becomes important above this frequency. The overall reduction of soil vibration rms provided by the USP is 3.6 dB, which is again a remarkable effect, though slightly lower than that provided by the ballast mat. Considering sleeper and ballast vibration, the use of the USP leaves unchanged with respect to case V1 the abatement of vibration from the ballast to the soil (14.5 dB), but improves the abatement from the sleeper to ballast (11.8 dB in case V6, against 8.3 dB in case V1). Finally, the combined use of BM and USP sums up the advantages provided by the two separate effects, and leads to a reduction of the rms soil vibration of 6.8 dB.

It should be noted that the reduction in soil vibration provided by cases V5–V7 is obtained by improving the vibration absorption/filtering properties of the track, rather than by reducing the impact effects at the crossing nose: this is demonstrated by the wheel overloading and unloading coefficients reported in Table 5, which remain practically the same as in the reference case V1. In particular, none of the considered track resilience modifications is able to suppress the loss of contact between the wheel and the rail. The time history of the vertical contact forces obtained in cases V5–V7 are not shown for brevity, but are very similar to those obtained in the reference case.

4.3. Combined effect of geometric correction and increase of track resilience

Before closing this section, the effect of combining the improvement of the local quality of rail geometry and the increase of track resilience is examined. Fig. 16a compares the $\frac{1}{3}$ octave band levels of rail vibration for the reference case V1 and for cases V8 (combination of profile correction, BM and USP) and V9 (same as V8 with additional correction of track geometry). The reduction of rail vibration with respect to the reference case is considerable, but almost no difference is observed between case V8 and V9, which confirms that track geometry correction is not effective in reducing impact at the crossing. The rms level of rail vibration is reduced for both case V8 and V9 by 7.5 dB with respect to the reference case: this is the largest improvement in rail vibration obtained in all cases considered.

Also for soil vibration (Fig. 16b), a very important reduction of vibration is obtained with respect to the reference case, but no advantage is brought by the use of TC. The rms of soil vibration is reduced by almost 10 dB, which is again the best result obtained over the entire sensitivity analysis, and the vibration abatement from the sleeper to ballast and from ballast to soil are similar to those obtained in case V7, where the use of BM and USP was not combined with rail profile correction.

5. Conclusions

In this paper, two approaches for modelling train–turnout interaction were compared and validated against measurements. The results of these comparisons have showed that both methods provide comparable results in terms of vertical acceleration on the crossing nose, in very good agreement with the corresponding measurements. It is important to underline that the three turnouts used for validation represent a rather wide range of possible train–turnout conditions in urban rail systems, with the RATP turnout representing the case of a subway turnout with vignole rails and relatively high train speed, while STIB and De Lijn represent two different cases of tramway applications. As previously discussed, these three examples correspond to different levels of track impact loading, so that the comparison may be considered representative of a wide variety of situations arising in urban railway turnout systems.

Although the two modelling approaches have been employed independently in this paper, an interaction between the two could also be envisaged. For example, Method A could be used to compute the time-varying position of contact point and different components of contact force, and these data could be used by Method B to compute vibration in the turnout and the soil. Another possibility would be to use Method A to "calibrate" the parameters (in particular the value of impact velocity) to be used by the impact excitation model in Method B.

The results of the sensitivity analysis illustrate the substantial influence of turnout geometry on impact effects generated by wheel passage over the crossing nose: with an ideal geometry of the crossing nose, loss of contact between the wheels and the rail at the crossing nose is avoided, and hence impact effects are noticeably lower than in the case of a degraded geometry. On the other hand, track geometry correction does not appear from the results of the sensitivity analysis as an effective mean to reduce impacts at the crossing. Further research would be desirable in order to improve the wear and damage resistance of the crossing nose surface, e.g. through use of new materials and/or optimised surface treatments.

The results of the parametric analysis also show that significant reduction of rail and especially of soil vibration levels can be achieved by increasing turnout resilience through insertion of a ballast mat, USPs, or possibly a combination of the two. When rail profile correction is combined with the increase of track resilience properties, large improvements of rail and soil vibration in the range of 7.5 dB for rail vibration and 10 dB for soil vibration are obtained.

Acknowledgement

The work reported herein was performed within the project TURNOUTS, funded by the European Community (contract number: TST3-CT-2003-505592).

References

[1] H. Netter, G. Schupp, W. Rulka, K. Schroeder, New aspects of contact modelling and validation within multibody system simulation of railway vehicles, *Vehicle System Dynamics* 28 (Suppl.) (1998) 246–269.
[2] S. Gurule, N. Wilson, Simulation of wheel–rail interaction in turnouts and special track work, *Vehicle System Dynamics* 33 (Suppl.) (2000) 143–154.
[3] J. Droździel, B. Sowinski, W. Groll, The effect of railway vehicle–track system geometric deviations on its dynamics in the turnout zone, *Vehicle System Dynamics* 33 (Suppl.) (2000) 641–652.
[4] C. Andersson, T. Dahlberg, Wheel/rail impacts at a railway turnout crossing, *Proceedings of the Institution of Mechanical Engineers Part F, Journal of Rail and Rapid Transit* 212 (1998) 123–134.
[5] C. Andersson, T. Dahlberg, Load impacts at railway turnout crossing, *Vehicle System Dynamics* 33 (1999) 131–142.
[6] E. Kassa, C. Andersson, J.C.O. Nielsen, Simulation of dynamic interaction between train and railway turnout, *Vehicle System Dynamics* 44 (2006) 247–258.
[7] E. Kassa, J.C.O. Nielsen, Dynamic interaction between train and railway turnout—full scale field test and validation of simulation models, *Vehicle System Dynamics* 28 (Suppl.) (1998) 521–534.
[8] E. Kassa, Dynamic Train–Turnout Interaction—Mathematical Modelling, Numerical Simulation and Field Testing, Thesis for the degree of Doctor of Philosophy, Chalmers University of Technology, Göteborg, Sweden, 2007.
[9] I. Anastasopoulos, S. Alfi, S. Bruni, A. Van Leuven, G. Gazetas, Advanced methods for the reduction of train impacts on urban turnouts: analytical evaluation and real-scale verification of new concepts, *10th International Conference on Application of Advanced Technologies in Transportation*, Athens (GR) May 27–31, 2008.
[10] P. Belforte, F. Cheli, R. Corradi, A Facchinetti, Software for the numerical simulation of tramcar vehicle dynamics, *Heavy Vehicle Systems—International Journal of Vehicle Design* 10 (2003) 48–69.
[11] G. Diana, F. Cheli, S. Bruni, A. Collina, Experimental and numerical investigation on subway short pith corrugation, *Vehicle System Dynamics* 28 (Suppl.) (1998) 234–245.
[12] J. Argyris, H.P. Mlejnek, *Dynamics of Structures*, North-Holland Publishing Company, Amsterdam, 1991.
[13] J. Piotrowski, H. Chollet, Wheel–rail contact models for vehicle system dynamics including multi-point contact, *Vehicle System Dynamics* 43 (2005) 455–483.
[14] Z.Y. Shen, J.K. Hedrick, J.A. Elkins, A comparison of alternative creep force models for rail vehicle dynamic analysis, *Vehicle System Dynamics* 12 (Suppl.) (1983) 79–82.
[15] F. Braghin, S. Bruni, G. Diana, Experimental and numerical investigation on the derailment of a railway wheelset with solid axle, *Vehicle System Dynamics* 44 (2006) 305–325.
[16] S. Alfi, S. Bruni, Mathematical model of train–turnout interaction, *Vehicle System Dynamics* 47 (5) (2009) 551–574.
[17] ORE Question B176—Cahier des charges pour un bogie a caractéristiques améliorées pour la circulation en courbe, Utrecht, Netherlands, 1989.